UNIVERSITY OF LEEDS

This is a repository copy of *Sparsity-based image monitoring of crystal size distribution during crystallization*.

White Rose Research Online URL for this paper:
http://eprints.whiterose.ac.uk/109425/

Version: Accepted Version

Article:

Liu, T, Hou, Y, Ma, CY orcid.org/0000-0002-4576-7411 et al. (1 more author) (2017) Sparsity-based image monitoring of crystal size distribution during crystallization. Journal of Crystal Growth, 469. pp. 160-167. ISSN 0022-0248

https://doi.org/10.1016/j.jcrysgro.2016.09.040

© 2016 Elsevier B.V. Licensed under the Creative Commons Attribution-NonCommercial-NoDerivatives 4.0 International
http://creativecommons.org/licenses/by-nc-nd/4.0/

Reuse
Unless indicated otherwise, fulltext items are protected by copyright with all rights reserved. The copyright exception in section 29 of the Copyright, Designs and Patents Act 1988 allows the making of a single copy solely for the purpose of non-commercial research or private study within the limits of fair dealing. The publisher or other rights-holder may allow further reproduction and re-use of this version - refer to the White Rose Research Online record for this item. Where records identify the publisher as the copyright holder, users can verify any specific terms of use on the publisher's website.

Takedown
If you consider content in White Rose Research Online to be in breach of UK law, please notify us by emailing eprints@whiterose.ac.uk including the URL of the record and the reason for the withdrawal request.

White Rose
university consortium
Universities of Leeds, Sheffield & York

eprints@whiterose.ac.uk
https://eprints.whiterose.ac.uk/

Sparsity-based image monitoring of crystal size distribution during crystallization

Tao Liu[a,*], Yan Huo[a], Cai Y. Ma[b], Xue Z. Wang[b,c]

[a]Institute of Advanced Control Technology, Dalian University of Technology, Dalian 116024, China
[b]Institute of Particle Science and Engineering, School of Chemical and Process Engineering, University of Leeds, Leeds LS2 9JT, UK
[c]School of Chemistry and Chemical Engineering, South China University of Technology, Guangzhou, China
* Corresponding author. E-mail: tliu@dlut.edu.cn; Tel: +86-411-84706465; Fax: +86-411-84706706

Abstract: To facilitate monitoring crystal size distribution (CSD) during a crystallization process by using an in-situ imaging system, a sparsity-based image analysis method is proposed for real-time implementation. To cope with image degradation arising from in-situ measurement subject to particle motion, solution turbulence, and uneven illumination background in the crystallizer, sparse representation of a real-time captured crystal image is developed based on using an in-situ image dictionary established in advance, such that the noise components in the captured image can be efficiently removed. Subsequently, the edges of a crystal shape in a captured image are determined in terms of the salience information defined from the denoised crystal images. These edges are used to derive a blur kernel for reconstruction of a denoised image. A non-blind deconvolution algorithm is given for the real-time reconstruction. Consequently, image segmentation can be easily performed for evaluation of CSD. The crystal image dictionary and blur kernels are timely updated in terms of the imaging conditions to improve the restoration efficiency. An experimental study on the cooling crystallization of α-type L-glutamic acid (LGA) is shown to demonstrate the effectiveness and merit of the proposed method.

Keywords: Crystallization process, crystal size distribution, real-time monitoring, image analysis, sparse representation, salience edge

1. Introduction

Monitoring the crystal size distribution (CSD) during a crystallization process is very important for control optimization to obtain the desired product quality and production efficiency [1]. With the rapid development of process analytical technology (PAT) in the past decade [2], a few real-time measurement methods have been explored for measuring CSD based on using the laser diffraction (LD), ultrasound attenuation (UA), and focused beam reflectance measurement (FBRM) technologies [3, 4]. In particular, FBRM has been increasingly applied for on-line monitoring of crystal size distribution termed as cord length distribution [5, 6], which is mainly effective for spherical particles. However, these technologies cannot offer two-dimensional details of crystal size or shape. By comparison, high-speed optical imaging devices have also been gradually adopted for crystal size measurement and shape identification in the recent years [2, 7]. Real-time image analysis has therefore become intensively appealed for monitoring crystallization processes.

Based on using an invasive or non-invasive imaging system for monitoring a crystallization process, a small number of real-time image analysis methods were explored for measuring crystal size or CSD [2]. By using a non-invasive imaging system, Larsen et al. [9] presented a model-based object recognition algorithm to extract crystal size information for the α-glycine crystallization process from the captured images; A synthetic image analysis method was developed for in-situ crystal type identification and size measurement in the recent paper [10]. By comparison, an invasive imaging system named particle vision and measurement (PVM) was adopted to develop a comprehensive image analysis [11] on the crystal size of monosodium glutamate during crystallization. In addition, a flow-through cell imaging device was used to estimate CSD [12], based on crystal image segmentation using the wavelet transform and fuzzy C-means clustering strategy. The device was further extended to take in-situ crystal images from two perpendicular directions [13], such that a faster image analysis algorithm was proposed to classify particles and count the particle sizes. A multivariate image analysis method was combined with a classical image technique for in-situ estimation of CSD [14]. To address the problem of out-of-focus particles provoking degraded imaging for in-situ monitoring, Presles et al. [15] developed an optimization strategy into the image analysis to acquire better particle characterization. To effectively extract the moving particle information for on-line measurement of particle size, Chen et al. [16] proposed a fast image processing algorithm for correction of imaging illumination and binarization in a two-phase flow. To tackle the recognized challenge of estimating the crystal growth rate from real-time captured images, a few advanced image processing techniques were presented to estimate the crystal length distribution specifically for needle-shaped crystals [17]. Agimelen et al. [18] adopted the mean aspect ratio of all the particles in the captured image by PVM to reduce the computation effort for particle size estimation. However, little work had been devoted to improve the captured image quality against the influence from the solution turbulence and time-varying illumination background with respect to the crystallization progress, which should be envisaged for effective particle extraction and CSD estimation during the crystallization process.

To eliminate the influence from particle motion, solution turbulence, uneven illumination background, and imaging noise, it is necessary to restore the true crystal images from the captured images in a fast manner. A synthetic sparsity-based image analysis strategy is therefore proposed in this paper for real-time monitoring of CSD with high efficiency and accuracy. Firstly, the noise in a captured crystal image is filtered out by using an image dictionary established in advance. Then the edges of a crystal shape in the captured image are determined in terms of the salience information defined from the denoised crystal images. These edges are used to determine the blur kernel for reconstruction of a denoised image. To this end, image segmentation is proceeded for evaluation of CSD subject to uneven illumination background. Experimental results are shown to demonstrate the proposed image analysis method for in-situ measurement of CSD for an L-glutamic acid (LGA) crystallization process.

2. Image analysis

Analysis of real-time crystal image aims at obtaining the details of CSD. The whole process of image analysis strategy for real-time CSD measurement is shown in Fig.1, including image preprocessing, image restoration, and image segmentation, which are presented in the following subsections, respectively.

2.1 Image preprocessing

In general, the size of a captured image depends on the resolution of an imaging system. Typically, when the size of a captured image becomes larger, a longer processing time is needed for on-line image analysis. To alleviate the time delay, an efficient method based on the wavelet transform [19] is adopted for downsizing the captured images while maintaining necessary information for real-time analysis. Given an original image $f(x, y)$ with the size $M \times N$, a two-dimensional discrete method is used for the wavelet transform based on the biorthogonal wavelet function [19]. Denote by m the row, by n the column, and by j the scale. The discrete wavelet transform for $f(x, y)$ is defined by

$$\begin{cases} A_{\varphi}(j,m,n) = \dfrac{1}{\sqrt{MN}} \displaystyle\sum_{x=1}^{M}\sum_{y=1}^{N} f(x, y)\varphi_{j,m,n}(x, y) \\ A_{\psi}^{i}(j,m,n) = \dfrac{1}{\sqrt{MN}} \displaystyle\sum_{x=1}^{M}\sum_{y=1}^{N} f(x, y)\psi_{j,m,n}^{i}(x, y),\ i = \{H, V, D\} \end{cases} \tag{1}$$

where

$$\begin{cases} \varphi_{j,m,n}(x, y) = 2^{j/2}\varphi(2^{j}x - m, 2^{j}y - m) \\ \psi_{j,m,n}^{i}(x, y) = 2^{j/2}\psi^{i}(2^{j}x - m, 2^{j}y - m),\ i = \{H, V, D\} \end{cases} \tag{2}$$

where $\psi_{j,m,n}^{i}(x, y)$, $i = \{H, V, D\}$ are used to identify three directional edges including horizontal, vertical, and diagonal directions, respectively. Then the original image $f(x, y)$ is decomposed into four parts at the scale j: a low frequency component $A_{\varphi}(j,m,n)$ which is used for approximating $f(x, y)$, and three high frequency components $A_{\psi}^{i}(j,m,n)$ to be removed.

2.2 Image restoration

Generally, a crystallization process is involved with solution agitation. Although a high-speed camera can be used to reduce the capture time for imaging, solution turbulence interferes with real-time imaging, causing difficulty to discern the outlines of crystals. To deal with the problem, a restoration algorithm is proposed to remove noise and blurs from the captured images, in order to facilitate the subsequent image segmentation and CSD measurement.

The key idea of image restoration is to establish a degradation model to recover the crystal images from the captured images, and then use a mathematical method of solving the inverse problem to obtain the optimal approximation of the original image. Due to that the related parameters (additive noise and blur kernel) could not be known in advance, a blind restoration method is explored here, including degradation model construction, image filtering, dictionary learning, salient edge estimation, blur kernel estimation, image deconvolution, as detailed in the following subsections.

2.2.1 Degradation model construction

It is assumed that in a captured crystal image with a short time exposure, the blur kernel is space-invariant. That is, the degradation model is simplified as

$$\mathrm{Y} = \mathrm{k} * \mathrm{X} + \mathrm{v} \tag{3}$$

where Y is a corrupted (i.e. captured) image, k a blur kernel, X a clean image, $*$ convolution operation, and v an additive noise.

Since there are three unknown variables in the model, it is proposed to iteratively solve them from (3) in terms of

$$\begin{cases} \mathrm{Y} = \mathrm{F} + \mathrm{v} \\ \mathrm{F} = \mathrm{k} * \mathrm{X} \end{cases} \tag{4}$$

In case the captured crytal images are vague and noisy due to solution turbulence, along with blurred image edges, a multi-scale scheme is suggested to improve the estimation accuracy of blur kernel. The unknown edge image $\nabla \mathrm{X}$ and blur kernel k are iteratively estimated by establishing an image pyramid model from a coarse scale (low resolution) to a fine scale (high resolution) with $\nabla \mathrm{F}$. Fig.2 shows the flowchart of the proposed restoration method based on a sparse representation.

2.2.2 Image filtering

For image filtering, the guided filtering algorithm [20] is adopted, and the guided image may be taken as a denoised image. When a denoised image is used, the guided filtering function is considered as an edge-protection filter, which preserves the image edge information. Moreover, the edge feature of the crystal image is distinguished by the guided filtering for better identification. For using the guided filtering, suppose the pixel $\mathrm{p_i}$ in the input image and the pixel $\mathrm{q_i}$ in the output image satisfying

$$\mathrm{q_i} = \alpha_\mathrm{k} \mathrm{p_i} + \beta_\mathrm{k}, \ \forall \mathrm{i} \in \omega_\mathrm{k} \tag{5}$$

where k is the index of the local square window ω_k which is taken as 51×51 in the input image, $(\alpha_\mathrm{k}, \beta_\mathrm{k})$ are the coefficients in ω_k which are determined by

$$(\alpha_\mathrm{k}, \beta_\mathrm{k}) = \arg\min_{\alpha_\mathrm{k}, \beta_\mathrm{k}} \sum_{\mathrm{i} \in \omega_\mathrm{k}} \left((\alpha_\mathrm{k} \mathrm{p_i} + \beta_\mathrm{k} - \mathrm{p_i})^2 + \varepsilon \alpha_\mathrm{k}^2 \right) \tag{6}$$

where ε is a tuning parameter which is taken as 0.01 in this work.

It follows from the filtering method [20] that

$$\alpha_\mathrm{k} = \frac{\frac{1}{|\omega|} \sum_{\mathrm{i} \in \omega_\mathrm{k}} \mathrm{p_i}^2 - \mu_\mathrm{k} \bar{\mathrm{p}}_\mathrm{k}}{\sigma_\mathrm{k}^2 + \delta} \tag{7}$$

$$\beta_\mathrm{k} = \bar{\mathrm{p}}_\mathrm{k} - \alpha_\mathrm{k} \mu_\mathrm{k} \tag{8}$$

where μ_k and σ_k^2 are the mean and variance of the input image in ω_k, $|\omega|$ is the total number of pixels in ω_k, and

$$\bar{p}_k = \frac{1}{|\omega|}\sum_{i\in\omega_k} p_i \tag{9}$$

The output image is therefore obtained by

$$q_i = \frac{1}{|\omega|}\sum_{i\in\omega_k} \alpha_k p_i + \beta_k \tag{10}$$

2.2.3 Dictionary learning

The goal of dictionary learning is to obtain the denoised image F shown in Eq.(4) in terms of the sparse representation. An important merit of dictionary learning is the robustness against an additive noise v, that is, learning from noisy images may provide a desired noise-free image dictionary. Inspired by the developed method [21], an effective dictionary learning algorithm of K-SVD is given as below,

Firstly, denote by Y an original image and by F the denoised image, a denoising model in the sparse domain [21] is established by

$$\left\{\hat{d}_{ij}, \hat{Y}\right\} = \arg\min_{z,q_{ij}} \lambda \| F - Y \|_2^2 + \sum_{i,j=1}^{M} \mu_{ij} \| d_{ij} \|_0 + \sum_{i,j=1}^{M} \| Ad_{ij} - R_{ij} F \|_2^2 \tag{11}$$

where d_{ij} are sparse representations of all the patches composing the original image, A the dictionary, M the size of dictionary, R_{ij} a matrix that extracts the (i, j) patch. The first term at the right-side of (11) denotes the global proximity between Y and F, the second term is a sparsity constraint with the coefficients μ_{ij}; The third term is related to the denoised image F, each patch denoted by $b_{ij} = R_{ij} F$ of size $\sqrt{n} \times \sqrt{n}$ has a sparse representation with a bounded error.

Then, a block coordinate-relaxation method is performed to update d_{ij}, using a windowed orthonormal matching pursuit (OMP) [21]. i.e.

$$\hat{d}_{ij} = \arg\min_{d} \mu_{ij} \| d \|_0 + \| Ad - b_{ij} \|_2^2 \tag{12}$$

Finally, the image dictionary is updated using the K-SVD method [22]. Iteration between the above two steps builds up a dictionary learning algorithm. Once converged, the denoised image F is computed by

$$\hat{F} = \left(\lambda I + \sum_{i,j=1}^{M} R_{ij}^T R_{ij}\right)^{-1} \left(\lambda Y + \sum_{i,j=1}^{M} R_{ij}^T A\hat{d}_{ij}\right) \tag{13}$$

2.2.4 Salient edge estimation

Owing to that CSD is measured from the image edges of the crystal particles, it is necessary to use the salient structure information of a denoised image to estimate the blur kernel. By extracting the structure information and filtering out the texture details from the denoised image F, blur kernel estimation is obtained in terms of an effective salient structure. Firstly, the salient structures are extracted by using a so-called relative-total-variation method [23]. The objective function for the input image F and the resulting structure image S is taken as

$$\mathrm{S}=\underset{\mathrm{S}}{\arg\min}\left\{\frac{1}{2}\|\mathrm{F}-\mathrm{S}\|_2^2+\lambda\sum_{\mathrm{i}}\left[\frac{\mathrm{D_m S(i)}}{\mathrm{L_m S(i)}+\varepsilon}+\frac{\mathrm{D_n S(i)}}{\mathrm{L_n S(i)}+\varepsilon}\right]\right\} \tag{14}$$

where i and j are indices of the 2D pixels, m and n pixel coordinates, λ a weight, and ε a small positive value used to avoid division by zero. Moreover, $\mathrm{g_{i,j}}$ is a specified Gaussian weighting function with the standard deviation σ relating to the spatial scale of the window, and $\mathrm{D_m S(i)}$ and $\mathrm{L_m S(i)}$ are total variations in the m and n directions for pixel i in the window, defined by

$$\begin{cases}\mathrm{D_m S(i)}=\sum\limits_{\mathrm{j}\in\mathrm{R(i)}}\mathrm{g_{i,j}}\,|(\partial_{\mathrm{m}}\mathrm{S})_{\mathrm{i}}| \\ \mathrm{L_m S(i)}=\sum\limits_{\mathrm{j}\in\mathrm{R(i)}}\mathrm{g_{i,j}}\,|(\partial_{\mathrm{m}}\mathrm{S})_{\mathrm{i}}|\end{cases} \tag{15}$$

Secondly, the edges of a denoised image should be sharpened for effective estimation. In this work, the shock filtering model [24] is used to improve the clarity of image edges.

Thirdly, the image edge $\nabla\mathrm{F}$ is estimated by using a gradient method based on a discrete filter, i.e.

$$\nabla\mathrm{F}=[\nabla_{\mathrm{m}}\mathrm{S},\nabla_{\mathrm{n}}\mathrm{S}] \tag{16}$$

where $\nabla_{\mathrm{m}}=[1,-1]$ and $\nabla_{\mathrm{n}}=[1,-1]^{\mathrm{T}}$.

2.2.5 Blur kernel estimation

For an original edge image denoted by $\nabla\mathrm{F}$ that may be blurred, image restoration is expressed by

$$\nabla\mathrm{F}=\mathrm{k}*\nabla\mathrm{X} \tag{17}$$

where $\nabla\mathrm{X}$ is unknown clean gradient image in the high frequency, and k is the blur kernel.

For iteration, a regularization function of $\mathrm{L_1/L_2}$ [25] is used to estimate the image $\nabla\mathrm{X_i}$ in the i th scale, the optimization objective function is defined as

$$\nabla\mathrm{X_i}=\underset{\nabla\mathrm{X_i}}{\arg\min}\frac{\lambda}{2}\|\mathrm{k_i}*\nabla\mathrm{X_i}-\nabla\mathrm{F_i}\|_2^2+\frac{\|\nabla\mathrm{X_i}\|_1}{\|\nabla\mathrm{X_i}\|_2} \tag{18}$$

where $\nabla\mathrm{F_i}$ and $\mathrm{k_i}$ are the original edge image and the blur kernel in the i th scale ($1\le\mathrm{i}\le\mathrm{S}$, where S is the index of the finest scale), and λ is used to make a compromise between the regularization and the scalar data.

With $\|\nabla\mathrm{X_i}\|_2$ determined by the previous iteration, Eq.(18) can be transformed into the following form [25],

$$\nabla X_i = \arg\min_{\nabla X_i} \frac{\lambda}{2} \| k_i * \nabla X_i - \nabla F_i \|_2^2 + \| \nabla X_i \|_1 \tag{19}$$

The fast iterative shrinkage threshold algorithm named as FISTA [26] is adopted for the inner iteration to solve the above minimization program.

Moreover, the blur kernel k_i is updated by solving the following minimization,

$$k_i = \arg\min_{k_i} \frac{\lambda}{2} \| k_i * \nabla X_i - \nabla F_i \|_2^2 + \| k_i \|_1 \tag{20}$$

An unconstrained iterative re-weighted least-squares (IRLS) method is used to solve the above problem, and the conjugate gradient method is used to ensure the convergence of IRLS [27].

For the multi-scale operation of successive approximation, when ∇X_i and k_i are computed by performing n_i interations in the i th scale, they are upsampled as the initial image and blur kernel of the finer scale $(i+1)$ by using the bicubic interpolation. Whereas, ∇F_i is downsampled from the original edge image ∇F . The size ratio is taken as $\sqrt{2}$ between the two adjacent scales in the multi-scale pyramid. Herein the size of ∇X_S is taken the same as that of ∇F , and the scale number S is determined by the blur kernel size in the first scale (e.g. an initial blur kernel size: 3×3). Note that the number of iteration n_i is defined as

$$\| k_i^{n_i} - k_i^{n_i-1} \|_2 \le \zeta, \; n_i > 1 \tag{21}$$

where $\zeta = 10^{-3}$ is taken in this work.

In addition, owing to that there are a lot of independent particles in a captured image, the blur kernel k_S should be optimized to remove the noise. A nonlinear filtering method [28] using a bilateral filter for noise removing and edge preserving is used to optimize the blur kernel k_S. As a result, the final blur kernel k is obtained by optimizing k_S.

2.2.6 Image deconvolution

After obtaining the blur kernel k , an image non-blind deconvolution algorithm based on a generalized iterated shrinkage algorithm [29] is used to obtain the clean image X by restoring the blurred image F with blur kernel k .

Considering that the blind restoration process may spend much time for on-line image processing, the dictionaries and blur kernels are updated timely in terms of the imaging conditions during crystallization, i.e. real-time image quality. In this paper, two assessment parameters (Tenengrad function [30] and mean gray value) are introduced to describe real-time image quality, that is, when both of these assessment parameters vary drastically (e.g. $|\text{change rate}| \ge 10\%$) between the current moment and the last updating moment for real-time monitoring, the dictionary and blur kernel will be updated for image restoration. For the image Y , Tenengrad function with the Sobel operator [30] is defined by

$$D(I) = \sum_m \sum_n \sqrt{I_m^2(m,n) + I_n^2(m,n)} \tag{22}$$

where m denotes the row, n the column, I_m and I_n are respectively the convolution of the input image $Y(m,n)$ with the sobel masks S_m and S_n, i.e.

$$\begin{cases} I_m = Y(m,n) * S_m \\ I_n = Y(m,n) * S_n \end{cases} \tag{23}$$

2.3 Image segmentation

To cope with uneven or low-contrast illumination background of captured crystal images, image enhancement is conducted to strengthen the region of interest (ROI), namely, crystal particles, which facilitates the subsequent image segmentation. The multi-scale retinex algorithm (MSR) [31] is therefore adopted to deal with images with poor visibility or low resolution, which had demonstrated superiority over previous methods.

After image enhancement, the minimum cross entropy segmentation algorithm [32] is performed, where the optimal threshold t^* is determined by computing the minimum cross entropy. Each segmented image is then used to extract the outlines of valid particles and remove the image background. Finally, a binary image I_b is obtained by

$$I_b(m,n) = \begin{cases} 0, & X(m,n) < t^* \\ 1, & X(m,n) \geq t^* \end{cases} \tag{24}$$

Through image segmentation, crystal sizes are computed by using the best fit rectangle method [33]. Note that the particle length and width are counted as the length and width of the best fit rectangle for the contour of a particle image. In this work, the length is considered as the key size for CSD estimation with respect to the crystal shapes of α- and β-form for LGA.

3. Experimental study

3.1 Experimental setup

A cooling crystallization experiment of α-type LGA was carried out based on using a non-invasive imaging system to demonstrate the efficiency of the proposed sparsity-based image analysis method for real-time CSD measurement. The experimental set-up for capturing the crystal images is shown in Fig.3. The crystallizer was composed of a 4L jacketed glass vessel, a 4-paddle agitator (PTFE), a temperature probe (Pt100), and a thermostatic circulator (product no.Julabo-CF41). The LGA solute and distilled water were used for experiment. A non-invasive imaging instrument including two high-speed cameras made by Hainan Six Sigma Intelligent Systems Ltd. (product no. Stereo Vision Crystal-G) was employed to take real-time crystal images during the cooling process. A LED light was used for illumination. Two high-resolution cameras (No. UI-2280SE-C-HQ) with CCD sensors were made by IDS Imaging Development Systems GmbH, which is able to take maximum 6 images per second. These images were in JPEG format with the pixel resolution of 2448×2050. The non-invasive imaging system was installed closely outside the cylindrical crystallizer. The camera flange focal distance was taken as 14.27 cm, and the shutter type was set as global with an exposure time of 0.11ms. An optical grid plate of of millimeter scale is used to adjust the focal length of the imaging system for in-situ measurement. In addition, a digital microscope (Leica DM 2500, LAS_v4.4) was used for CSD validation.

3.2 Image analysis results

Real-time images were captured at the sequential time points subject to particle motion, solution turbulence and uneven illumination background during the cooling crystallization process. Note that the illumination intensity was gradually reduced with the increment of crystals during crystallization. Fig.4a shows a captured image subject to the LGA solution agitation at a paddle stirring speed of 250 rpm and uneven illumination. It is seen that the contours of particle shapes were severely blurred. It should be noted that the focal length of the imaging system had been properly adjusted to guarantee no image blurring under no agitation of the crystallizer, while the image distortion was negligible for in-situ measurement.

The proposed image preprocessing and restoration methods were implemented for the captured images. Fig.4b shows the performance of image restoration on the captured images. It is seen that the influence from particle motion, solution turbulence and uneven illumination background is almost eliminated.

For comparison, the developed blind deconvolution method [25] was also used for the same captured image. The comparison result is shown in Fig.5. It is seen that most of the particles have been well restored by the proposed restoration method. In contrast, the edges of some particles as outlined by the yellow circle are less distinct by using the cited method [25] as shown in Fig.5b. Moreover, the blur kernel is estimated with a smaller number of discrete noisy points as shown by Fig.5c, compared to that obtained by the cited method [25] as shown by Fig.5d. The commonly used quantitative indicators of image quality [30], Tenengrad, Brenner, and energy gradient, are computed for comparison. The results are listed in Table 1 (the larger is the better), indicating further improved image quality is obtained by the proposed method.

For the restored image shown in Fig.4b, the pixel intensity with respect to the image width and length is plotted in Fig.6a, which indicates that the crystal image is heavily subject to uneven imaging background, causing difficulty to the subsequent image segmentation. The result of image enhancement is shown in Fig.6b, demonstrating that most of the particles are highlighted compared to the original or restored image shown in Fig.4. Then the proposed segmentation method is applied to the image with uneven pixel intensity, obtaining the segmentation result shown in Fig.6c.

Due to the fact that particles are inevitably subject to breakage and agglomeration during the crystallization process, tiny particles including those arising from particle breakage, together with the agglomerated particles, should not be counted for properly estimating the CSD during the crystallziation process. It is therefore necessary to sieve out valid particles from the restored image to ensure effective estimation of CSD. The particle sieving method developed in the recent paper [10] is adopted to extract valid particles from the segmented image, as shown in Fig.6d, by specifying the minimum number of pixels larger than 100 for each particle (to exclude tiny particles) and the concave-convex degree higher than 0.75 (to exclude agglomerated particles).

Note that the total time spent for the image restoration by the proposed method coded by MATLAB (version 2013a) was smaller than 3 seconds in terms of a computer configured with CPU of Intel 3.40 GHZ and RAM of 8.00G, based on the established blur kernels and dictionary learning. The time spent for particle sieving and computation of CSD is smaller than 1 second based on the image restoration.

3.3 CSD estimation results

To demonstrate the effectiveness of the proposed sparsity-based image analysis for real-time monitoring, another offline measurement using an electric microscope was performed. Before the real-time experiment of CSD estimation, the LGA solution was first heated up to 75°C and the temperature was held for one hour to guarantee that all the LGA solutes were completely dissolved. The solution was then cooled down to 45°C at a fast cooling rate of 0.8°C/min. The crystal seeds were poured into the solution at the temperature 45°C, of which the CSD was measured beforehand with an electric microscope for comparison. In-situ images were captured within 15 seconds after the seeding. Note that the crystal length distribution remained almost unchanged during the short time interval. Subsequently, a slow cooling rate of 0.2°C /min was maintained in the experiment. Totally after 60 minutes, in-situ images of the crystal solution were once again captured within another 15 seconds. Then the crystals were immediately sampled from the crystallizer and dried for offline measurement by using an electric microscope. It was found that the averaged changing rates of Tenengrad function and mean gray value for real-time image anlysis from the beginning to the end of experiment were about -24% and -53%, respectively. Correspondingly, the dictionaries and blur kernels for image restoration were apparently different with respect to the crystal growth process. Hence, the experiment is suitable for demonstrating the effectiveness of the proposed method for on-line monitoring.

Fig.7 shows the image analysis results of LGA CSD in length given by the proposed method and the offline measurement. The CSDs were counted based on almost 500 particles from the images captured within 15 seconds around $t = 0\,\text{min}$ and $t = 60\,\text{min}$, respectively. It is seen that the analysis results are very similar by using these two methods. To clarify the similarity, define the relative error of L_1-norm distance (abbreviated by L_1ND) between two vectors $\mathbf{a}$ and $\mathbf{b}$ in an ascending or descending order by

$$E_{L_1ND} = \frac{1}{N}\sum_{i=1}^{N}\frac{|\mathbf{a}_i - \mathbf{b}_i|}{|\mathbf{b}_i|} \tag{25}$$

The relative errors of mean size (MS), standard deviation (SD), and L_1ND for the LGA CSD in length by using the proposed method in contrast with the offline measurement are listed in Table 2, where T1 denotes $t = 0\,\text{min}$, and T2 is $t = 60\,\text{min}$. The results demonstrate that the image analysis results given by the proposed real-time method are very close to those of the offline measurement.

4. Conclusions

A synthetic image monitoring method based on a sparse representation has been proposed for real-time CSD estimation during a crystallization process, which can accommodate for poor imaging conditions including particle motion, solution turbulence, and uneven illumination background. An image restoration method is proposed to restore the corrupted images captured from an on-line non-invasive imaging system for monitoring crystal growth. By introducing two assessment parameters of real-time image quality, the image dictionary and blur kernels are timely updated to improve the restoration quality while saving the processing time. A non-blind deconvolution algorithm has been given for real-time reconstruction, such that image segmentation can be conveniently conducted to estimate CSD. Experiment results have demonstrated that the proposed sparsity-based image analysis can be effectively used for real-time monitoring of CSD, very close to the offline measurement by using an electric microscope. Nevertheless, it should be noted that two-dimensional analysis of CSD has certain limitation to reflect the growth of faceted crystals. It is therefore desired to develop a three-dimensional reconstruction strategy for CSD estimation in the future work.

Acknowledgments

This work is supported in part by the National Thousand Talents Program of China, NSF China Grants 61473054, 61633006, and 21306017, and the Fundamental Research Funds for the Central Universities of China.

References

[1] M. Li, D. Wilkinson, K. Patchigolla, Determination of non-spherical particle size distribution from chord length measurements. Part 2: Experimental validation, Chemical Engineering Science 60 (2005) 4992-5003.

[2] Z.K. Nagy, G. Fevotte, H. Kramer, et al., Recent advances in the monitoring, modeling and control of crystallization systems, Chemical Engineering Research & Design 91 (2013) 1903-1922.

[3] A. Ruf, J. Worlitschek, M. Mazzotti, Modeling and experimental analysis of PSD measurements through FBRM, Particle & Particle Systems Characterization 17 (2000) 167-179.

[4] M.R. Singh, J. Chakraborty, N. Nere, et al., Image-analysis-based method for 3D crystal morphology measurement and polymorph identification using confocal microscopy, Crystal Growth & Design 12 (2012) 3735-3748.

[5] M. Li, D. Wilkinson, K. Patchigolla, Obtaining particle size distribution from chord length measurements, Particle & Particle Systems Characterization 23 (2006) 170-174.

[6] H. Li, Y. Kawajiri, M.A. Grover, et al. Application of an empirical FBRM model to estimate crystal size distributions in batch crystallization, Crystal Growth & Design 14 (2014) 607-616.

[7] X.Z. Wang, K.J. Roberts, C. Ma, Crystal growth measurement using 2D and 3D imaging and the perspectives for shape control, Chemical Engineering Science 63 (2008) 1173-1184.

[8] R. Zhang, C. Ma, J. Liu, et al., On-line measurement of the real size and shape of crystals in stirred tank crystalliser using non-invasive stereo vision imaging, Chemical Engineering Science 137 (2015) 9-21.

[9] P.A. Larsen, J.B. Rawlings, N.J. Ferrier, Model-based object recognition to measure crystal size and shape distributions from in situ video images, Chemical Engineering Science 62 (2007) 1430-1441.

[10] Y. Huo, T. Liu, H. Liu, C.Y. Ma, X.Z. Wang, In-situ crystal morphology identification using imaging analysis with application to the L-Glutamic acid crystallization, Chemical Engineering Science 148 (2016) 126-139.

[11] Y. Zhou, R. Srinivasan, S. Lakshminarayanan, Critical evaluation of image processing approaches for real-time crystal size measurements, Computers & Chemical Engineering 33 (2009) 1022-1035.

[12] B. Zhang, A. Abbas, J.A. Romagnoli, Multi-resolution fuzzy clustering approach for image-based particle characterization for particle systems, Chemometrics & Intelligent Laboratory Systems 107 (2011) 155-164.

[13] S. Schorsch, T. Vetter, M. Mazzotti, Measuring multidimensional particle size distributions during crystallization, Chemical Engineering Science 77 (2012) 130-142.

[14] D. Sarkar, X.T. Doan, Y. Zhou, et al., In situ particle size estimation for crystallization processes by multivariate image analysis, Chemical Engineering Science 64 (2009) 9-19.

[15] B. Presles, J. Debayle, G. Févotte, et al., Novel image analysis method for in situ monitoring the particle size distribution of batch crystallization processes, Journal of Electronic Imaging 19 (2010) 0312071-0312077.

[16] X. Chen, W. Zhou, X Cai, et al., In-line imaging measurements of particle size, velocity and concentration in a particulate two-phase flow, Particuology 13 (2014) 106-113.

[17] J.X. Wu, S.V. Kucheryavskiy, L.G. Jensen, et al., Image analytical approach for needle-shaped crystal counting and length estimation, Crystal Growth & Design 15 (2015) 4876-4885.

[18] O.S. Agimelen, A. Jawor-Baczynska, J. McGinty, et al., Integration of in situ imaging and chord length distribution measurements for estimation of particle size and shape, Chemical Engineering Science 144 (2016) 87-100.

[19] R.C. Gonzalez, R.E. Woods, S.L. Eddins, Digital image processing using MATLAB, Prentice Hall, Upper Saddle River, NJ, 2004.

[20] K. He, J. Sun, X. Tang, Guided image filtering, IEEE Transactions on Pattern Analysis & Machine Intelligence 35 (2013) 1397-1409.

[21] M. Elad, M. Aharon, Image denoising via sparse and redundant representations over learned dictionaries, IEEE Transactions on Image Processing 15 (2006) 3736-3745.

[22] M. Aharon, M. Elad, A. Bruckstein, K-SVD: An algorithm for designing overcomplete dictionaries for sparse representation, IEEE Transactions on Signal Processing 54 (2006) 4311-4322.

[23] L. Xu, Q. Yan, Y. Xia, J. Jia, Structure extraction from texture via relative total variation, ACM Transactions on Graphics 31 (2012) 439-445.

[24] G. Gilboa, N.A. Sochen, Y.Y. Zeevi, Regularized shock filters and complex diffusion, European Conference on Computer Vision 2350 (2002) 399-413.

[25] D. Krishnan, T. Tay, R. Fergus, Blind deconvolution using a normalized sparsity measure, IEEE Conference on Computer Vision and Pattern Recognition (2011) 233-240.

[26] A. Beck, M. Teboulle, A fast iterative shrinkage-thresholding algorithm for linear inverse problems, SIAM Journal on Imaging Sciences 2 (2009) 183-202.

[27] A. Levin, R. Fergus, F. Durand, et al., Image and depth from a conventional camera with a coded aperture, ACM Transactions on Graphics 26 (2007) 701-709.

[28] C. Tomasi, R. Manduchi, Bilateral filtering for gray and color images, IEEE International Conference on Computer Vision (1998) 839-846.

[29] W. Zuo, D. Meng, L. Zhang, et al., A generalized iterated shrinkage algorithm for non-convex sparse coding, IEEE International Conference on Computer Vision (2013) 217-224.

[30] J.L. Pech-Pacheco, G. Cristóbal, J. Chamorro-Martínez, et al. Diatom autofocusing in brightfield microscopy: a cmparative study, International Conference on Pattern Recognition 3 (2000) 314-317.

[31] Z.U. Rahman, D.J. Jobson, G.A. Woodell, Multi-scale retinex for color image enhancement, IEEE International Conference on Image Processing 3 (1996) 1003-1006.
[32] C.H. Li, C.K. Lee, Minimum cross entropy thresholding, Pattern Recognition 26 (1993) 617-625.
[33] W. Wang, Image analysis of particles by modified ferret method: best-fit rectangle, Powder Technology 165 (2006) 1-10.

List of Table and Figure Captions

Table 1 Comparison of image quality via quantitative indicators

Table 2 Relative errors of CSD between the proposed real-time measurement and the offline measurement

Fig.1 The flow chart of image analysis

Fig.2 The restoration procedure for a captured crystal image

Fig.3 Experimental set-up for cooling crystallization of LGA

Fig.4 Crystal image restoration: (a) captured image; (b) restored image

Fig.5 Comparison of image processing results: (a) the proposed method; (b) the blind deconvolution method [25]; (c) the blur kernel by the proposed method; (d) the blur kernel by the blind deconvolution method [25].

Fig.6 Image segmentation result under uneven illumination background: (a) 2D plot of pixel intensity; (b) enhanced image; (c) segmented image; (d) valid particles extracted from the segmented image

Fig.7 Analysis of LGA CSD in length: (a) result at $\mathrm{t} = 0\,\mathrm{min}$ by the proposed method; (b) result at $\mathrm{t} = 0\,\mathrm{min}$ by offline measurement; (c) result at $\mathrm{t} = 60\,\mathrm{min}$ by the proposed method; (d) result at $\mathrm{t} = 60\,\mathrm{min}$ by offline measurement

Table 1 Comparison of image quality via quantitative indicators

Quantitative indicators	Tenengrad	Brenner	Energy gradient
Fig.5a	53.97	346.91	227.80
Fig.5b	53.13	318.58	214.95

Table 2 Relative errors of CSD between the proposed real-time measurement and the offline measurement

CSD data	Relative error (%)		
	MS	SD	L_1 ND
T1	1.91	5.57	3.18
T2	5.31	12.82	9.37
Average	3.61	9.20	6.27

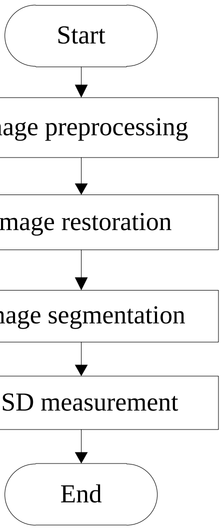

Fig. 1. The flow chart of image analysis

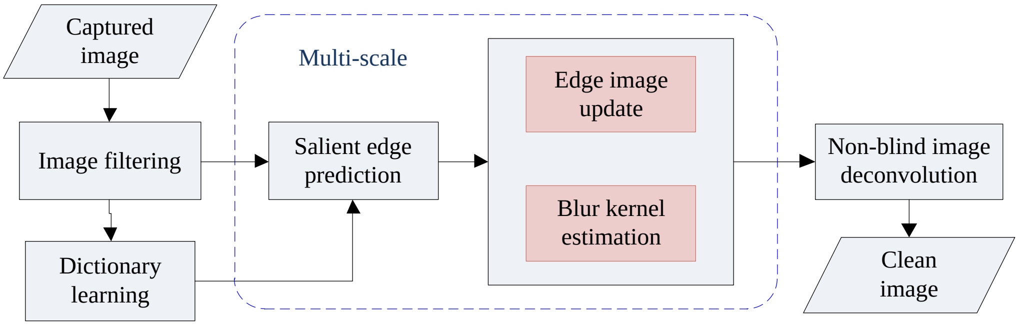

Fig. 2. The restoration procedure for a captured crystal image

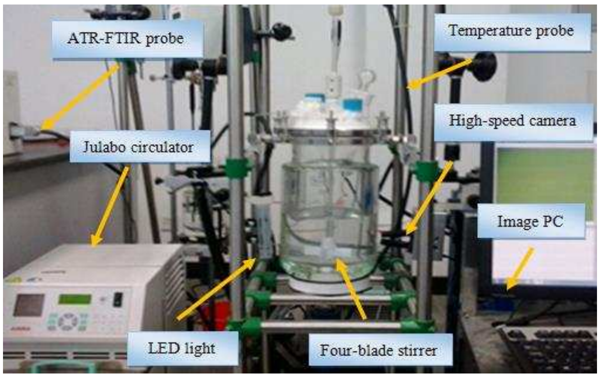

Fig. 3. Experimental set-up for cooling crystallization of LGA

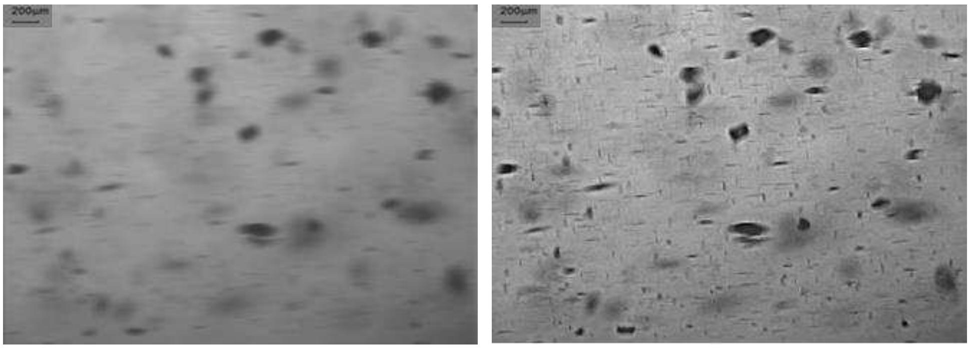

(a) **(b)**

Fig. 4. Crystal image restoration: (a) captured image; (b) restored image.

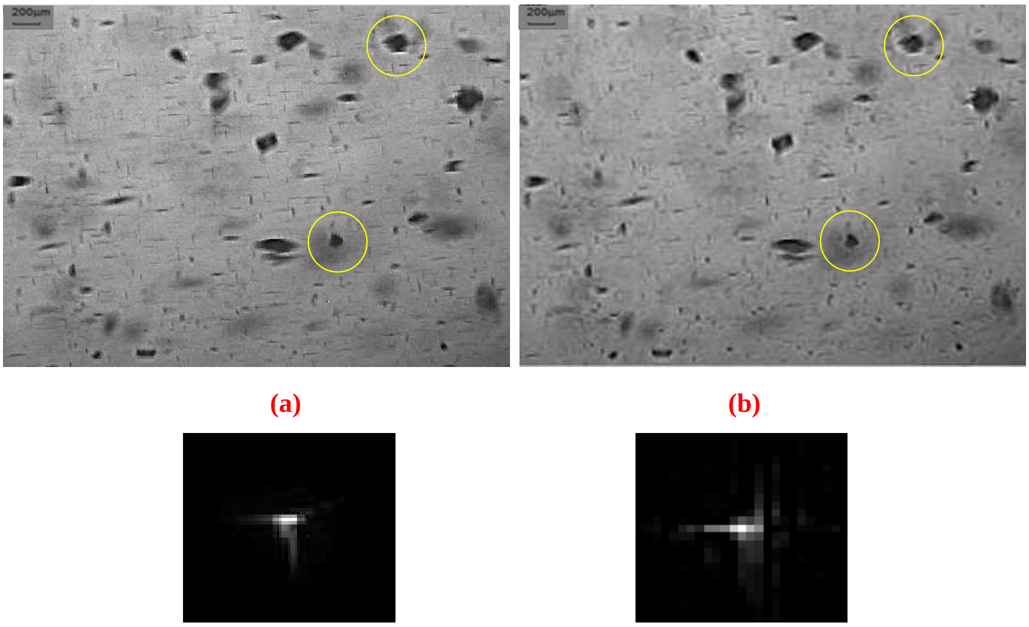

(a) **(b)**

(c) **(d)**

Fig. 5. Comparison of image processing results: (a) the proposed method; (b) the blind deconvolution method [25]; (c) the blur kernel by the proposed method; (d) the blur kernel by the blind deconvolution method [25].

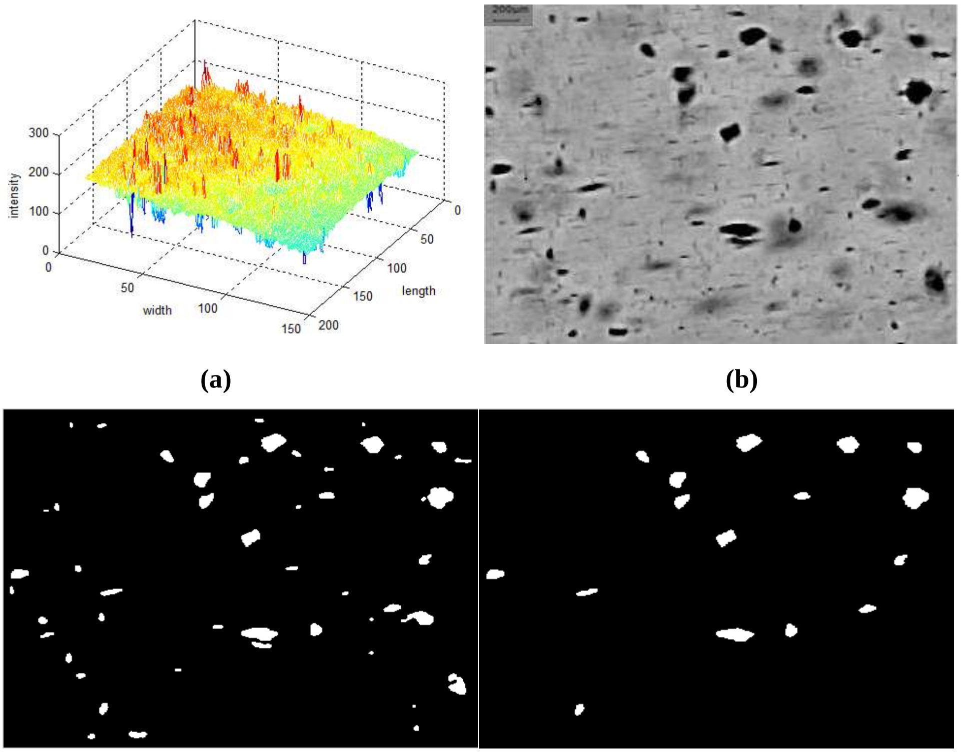

(a) (b)

(c) (d)

Fig. 6. Image segmentation result under uneven illumination background: (a) 2D plot of pixel intensity; (b) enhanced image; (c) segmented image; (d) valid particles extracted from the segmented image.

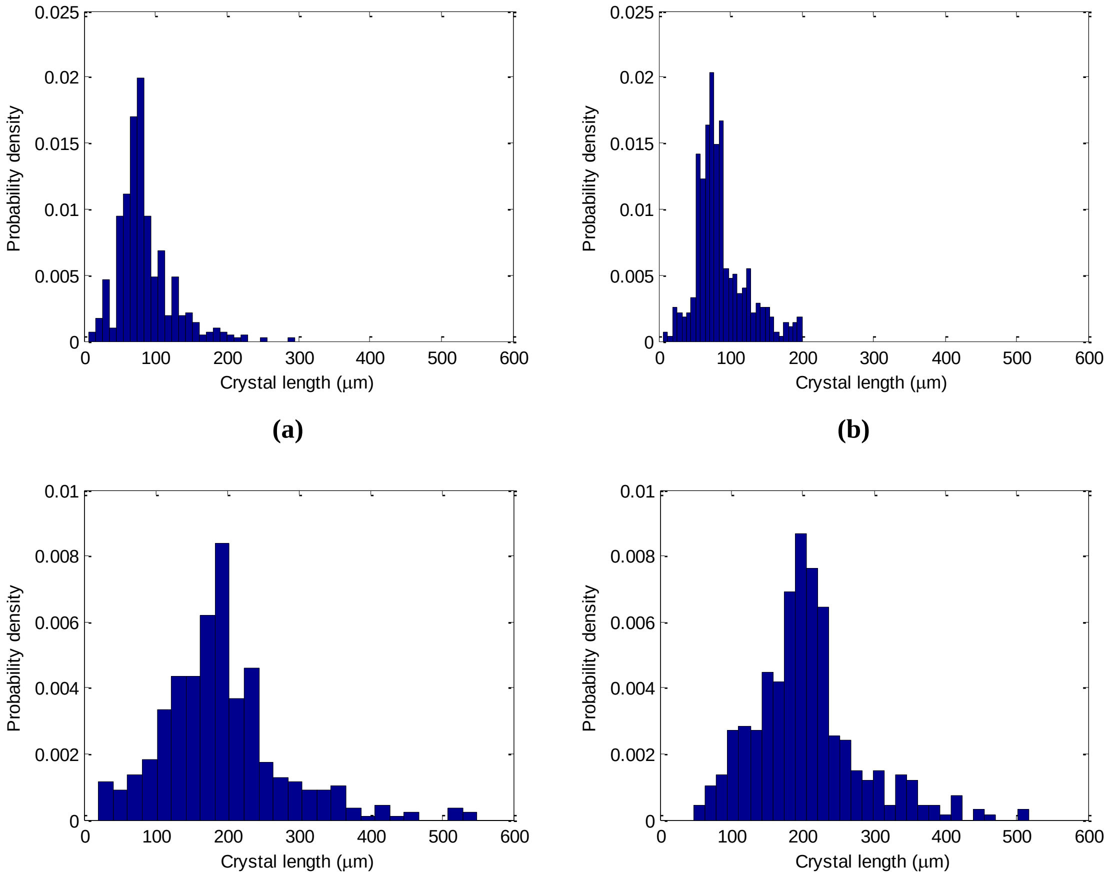

(a) (b)

(c) (d)

Fig. 7. Analysis of LGA CSD in length: (a) result at $t = 0\,\mathrm{min}$ by the proposed method; (b) result at $t = 0\,\mathrm{min}$ by offline measurement; (c) result at $t = 60\,\mathrm{min}$ by the proposed method; (d) result at $t = 60\,\mathrm{min}$ by offline measurement